Time-Resolved X-Ray Imaging of Aluminum Alloy Solidification Processes

RAGNVALD H. MATHIESEN, LARS ARNBERG, KJELL RAMSØSKAR, TIMM WEITKAMP, CHRISTOPH RAU, and ANATOLY SNIGIREV

Time-resolved direct-beam X-ray imaging, with intense, coherent, and monochromatic third-generation synchrotron radiation, and a high-resolution fast-readout detector system have been used for *in-situ* studies of dendritic and eutectic growth processes in Al-Cu alloys. Temporal and spatial resolutions down to 0.25 seconds and 2.5 μm, respectively, were obtained with a field of view up to 1.4 $\times$ 1.4 mm^2. Solid-liquid interfaces and various phase-specific segregates could be observed, and their dynamics could be traced in a sequence of temporally resolved images formed by phase and amplitude contrast from the sample. This article does not present any detailed analysis of a specific solidification phenomenon; instead, it presents to the scientific community an innovative technique for *in-situ* monitoring of such a phenomenon in real metallic systems.

I. INTRODUCTION

DEMANDING applications in the automotive industry call for aluminum castings to be mass produced without casting defects. Predictive models for heat and fluid flow are successfully being used in the design of components and casting processes, but the ability of those models to quantitatively predict casting defects such as porosity and hot tearing is limited. One example is the calculation of interdendritic feeding, which is essential in many types of casting-defect modeling. This requires accurate values of the interdendritic permeability, which is a function of the fraction and morphology of the dendrite phase.[1] Existing models for dendritic growth do not predict morphological parameters with sufficient accuracy for reliable permeability calculations.[2] The present lack of knowledge of the morphological development of aluminum alloy microstructures during solidification is, thus, prohibitive for the development of the sophisticated casting models that are needed in the aluminum foundry industry.

Several experimental methods have been used to investigate how the microstructure develops during solidification. A metallographic investigation of the solidified material shows a microstructure which has transformed and coarsened during the solidification and subsequent cooling, and it is often difficult to conclude how the growing crystals have evolved during the early stages of solidification.

Quenching of the microstructure during solidification results in a substantial refinement, and this method has been used in order to "freeze" the microstructure. Subsequent metallographic investigation shows a coarse structure, which is assumed to be representative of the solid at the moment of quenching, and a fine microstructure which is assumed to represent the melt. Transient phenomena in the destabilization of the growing microstructure subsequent to the quenching, however, result in a gradual transformation from the coarse to the fine microstructure, and this often leads to errors such as *e.g.*, an over estimation of the fraction of solid.[3]

Another method to obtain an impression of the microstructure during solidification is decanting or drainage of the melt during solidification and subsequent investigation of the solidified crystal network. Drainage sometimes takes place naturally in aluminum castings due to insufficient feeding, but it can also be promoted. This method, however, is limited to relatively coarse, coherent structures.

Transparent organic materials have successfully been used to simulate the solidification of metals.[4] These organic materials have low entropies of fusion and, therefore, solidify in a nonfaceted way like metals. Since they are transparent, growing crystals can be studied under the microscope due to phase contrast at the solid-liquid interface. These so-called transparent analogs have been used to study the morphology of cellular, dendritic, and eutectic solidification. Even though the information from such studies has been useful to verify theories on cellular and dendritic morphology, the information that can be achieved is limited. First, only a limited number of organic substances can be used. These materials are, of course, not representative of all metallic alloy systems, with their different constitutions and microstructures. Therefore, there are important and complex systems, like the aluminum-silicon eutectic, which cannot be simulated realistically with any analog system. Second, the phase-contrast image is limited to the solid/liquid interface. Apart from very special cases,[5] where model systems can be alloyed with optically opaque elements, variations in alloy composition in the solid and liquid are not visible, which means that solute boundary layers in the melt, micro-, and macrosegregation cannot be studied. Moreover, no efficient grain-refinement method has been found for transparent analog materials; hence, nucleation and early stages of equiaxed growth cannot be studied.

In-situ monitoring of solidification processes in metals and alloys has been carried out with several different methods utilizing X-ray exposure. Direct-beam X-ray microscopy

RAGNVALD H. MATHIESEN, Research Scientist, is with SINTEF Materials Technology, N-7465 Trondheim, Norway, Contact e-mail: Ragnvald.Mathiesen@sintef.no LARS ARNBERG, Professor, Department of Electrochemistry and Metallurgy, and KJELL RAMSØSKAR, Retired Research Scientist, Department of Physics, are with the Norwegian University of Science and Technology, N-7491 Trondheim, Norway. TIMM WEITKAMP, Ph.D Student, CHRISTOPH RAU, Postdoctor, and ANATOLY SNIGIREV, Beamline Scientist, are with the Experiments Division, ESRF, F-38043, Grenoble, France.

Manuscript submitted October 3, 2001.

measurements have been used to characterize solidification processes in terms of spatiotemporal variations in attenuation of the X-ray field by the material.[6–9] However, these methods, by utilizing image contrast from a local variation in absorption, require relatively large constitutional differences between different regions to be resolvable by contrast. Consequentially, the methods are not applicable to *in-situ* studies of solid-liquid–front morphologies and propagation in general, but are limited to systems in which the two phases can be distinguished from an adequately sharp transition in the X-ray attenuation between the separate phase domains. Also, the extraction and storage of quantitative pixel-by-pixel data, in work where high resolutions in both time and space are required, demand specially constructed detector systems with a high signal-to-noise ratio over a large part of the dynamic range of the detector. This enables the incident X-ray photon energy to be selected not only to ensure adequate transmission, but also in order to optimize image contrast.

Planar, cellular, and dendritic growth processes in various alloys have been studied *in-situ* using synchrotron X-ray topography,[10,11] but this experimental method is limited to studies of morphological structures at a subminute-to-minute temporal resolution. The applicability as a method to reveal detailed information on phase-front propagation and complex morphologies is, therefore, limited, and its output is not comparable to the detailed information obtained from light microscopy on transparent analogs.

A new method, in which high-energy synchrotron X-rays are used for *in-situ* direct-beam imaging of solidification processes, was recently developed and demonstrated to be successful in studies of alloys from the tin-lead system.[12,13] With a high-brilliance, transversely coherent monochromatic X-ray beam and a high-resolution fast-readout detector, the dynamics of propagating solid-liquid interfaces as well as the formation and behavior of phase-specific macrosegregation in Sn-Pb and Pb-Sn alloys could be studied, with temporal resolutions of about 0.7 seconds and spatial resolutions down to 5.0 μm. Due to the relatively low X-ray transmission in Sn, and even more strongly so in Pb, over the energy range available, these resolutions were predominantly limited by the samples. Therefore, it became a motivation for further studies to change the alloying system toward a system with less-attentuating elements.

The Al-Cu system has been extensively studied as a model system for aluminum-alloy microstructure development.[1,3,14] Both Al and Cu are well-suited elements with respect to X-ray transmission and temporal resolution, yet with large enough differences in their X-ray attenuation lengths to have the potential of giving contrast from segregated sample domains. The present article reports results from X-ray imaging studies of solidification in Al-Cu alloys.

II. EXPERIMENTAL

A. *Principles of X-ray Transmission Imaging*

In direct-beam imaging, X-ray interaction with matter is governed by the refractive properties of the material. Refraction of an incident monochromatic wave, at the boundary of a homogeneous domain, **r**, in the material, is characterized by the refractive index $n_{\mathbf{r}}$, which can be expressed as[15]

$$n_{\mathbf{r}} = 1 - \delta_{\mathbf{r}} - i\beta_{\mathbf{r}}, \qquad [1]$$

where the real part, $1 - \delta_{\mathbf{r}}$, describes refraction, whereas the imaginary part, $i\beta_{\mathbf{r}}$, is due to the absorption of the electromagnetic wave. The refractive index of vacuum is $n_{\text{vac}} \equiv 1$. For a monoatomic and homogeneous domain, $\delta_{\mathbf{r}}$ is given by the expression

$$\delta_{\mathbf{r}} = \frac{\lambda^2 r_0}{2\pi}\rho(Z + f'), \qquad [2]$$

where λ is the wavelength of the incident beam, r_0 is the classical electron radius, and ρ is the atomic density of the material. Z is the atomic number, and f' is the real part of the atomic anomalous scattering factor, accounting for resonance effects on the scattering amplitude when the incident photon energy is close to a photoelectric absorption edge. The magnitude of the imaginary part in Eq. [1] can be given as

$$\beta_{\mathbf{r}} = \lambda\frac{\mu}{4\pi} = \lambda\frac{\rho\sigma_a}{4\pi}, \qquad [3]$$

where μ and σ_a are the linear absorption coefficient and the absorption cross section, respectively, of the domain. σ_a varies approximately as λ^3 between photoelectric absorption edges, where it is discontinuous, and varies with the atomic number roughly as Z^4 at a fixed photon energy.

Comparing Eqs. [2] and [3], one finds that for a fixed wavelength, $\delta \propto \rho Z$, whereas $\beta \propto \rho Z^4$. Hence, refraction is more sensitive than absorption for making contrast from boundary regions of similar atomic compositions but of different densities. Selection of a suitable photon energy for an imaging experiment becomes a compromise between optimizing element and density contrasts while ensuring adequate sample transmission. Typical numerical values of δ for any material in the hard X-ray ($\lambda \leq 1.0$ Å) regime are between 10^{-5} and 10^{-6}; accordingly, the refractive properties for X-rays by any material deviate only slightly from n_{vac}, the material X-ray optical density being less than that of vacuum.

Let the sample be surrounded by vacuum and assumed to be built up as a continuum of bounded and homogeneous, but not necessarily monoatomic, regions. Let $\mathbf{E}_i(x, y, z)$ be a incident-plane wave propagating along the x-axis in a Cartesian laboratory coordinate frame. The transverse cross sections of the incident-wave field, $\mathbf{E}_i(y, z)$, and the wave field transmitted through the sample, $\mathbf{E}(y, z)$, can be related through the sample transmission function, $F(y, z)$:[16]

$$\mathbf{E}(y, z) = F(y, z)\mathbf{E}_i(y, z), \qquad [4]$$

with

$$F(y, z) = A(y, z)\exp(i\phi(y, z)).$$

The amplitude, $A(y, z)$, and the phase, $\phi(y, z)$, can be defined in terms of the refractive properties of the sample:

$$A(y, z) = \exp\left(-\frac{2\pi}{\lambda}\int \beta(x, y, z)dx\right), \qquad [5]$$

$$\phi(y, z) = -\frac{2\pi}{\lambda}\int \delta(x, y, z)dx. \qquad [6]$$

From these expressions, it is seen that attenuation of the beam along x for any given (y, z) results in an amplitude contrast, $A(y, z)$, directly traceable in the structure of the transmitted wave amplitude, $|\mathbf{E}(y, z)|$. Refraction results in

local phase shifts in the transmitted wave field and can, therefore, only be detected if the refracted waves are allowed to interfere with each other or, more commonly, with an unperturbed wave.[17] Such interference effects are referred to in microscopy as phase contrast.

In order to detect interference between an unperturbed wave field and waves refracted by the sample, the wave must be coherent over a relatively large cross section with respect to its wave length, due to physical limits in resolution. The resolution of modern X-ray detector systems and light microscopes are both typically in the submicron regime. Requirements for longitudinal coherence, which depends solely on monochromaticity, can be met quite easily. The transverse coherence, however, must be of the order of ≥ 10 μm, in order to give detectable interference effects. While this requires visible light coherence of the order of 100 periods, a 10 μm transverse coherence of a 1 Å X-ray beam requires a wave front in phase over 10^5 periods. This is not easily achieved while simultaneously maintaining a high photon flux, a prerequisite for applying transmission-beam imaging in studies of dynamic systems. Such contradicting requirements can, in general, only be met by third-generation synchrotrons, where a small source size and beam divergence enables a transverse coherence of several tenths of micrometers without excessive use of beam-defining apertures.

B. *The Experimental Setup*

1. *The characteristics of the X-ray source and optical elements*

The experiments were carried out in the second experimental hutch (EH2) of the μ-FID beamline (ID22) at the European Synchrotron Radiation Facility. The ID22 source is an undulator located at a so-called high-beta straight section, where the magnetic lattice of the electron-beam storage ring is operated to optimize the photon-source characteristics of the undulator, yielding a high brightness, narrow bandwidths, and low divergences. The full-width half-maximum (FWHM) optical-source size at ID22 is typically 0.7×0.03 mm^2 (horizontal $\times$ vertical) with FWHM divergence of 30×20 μrad^2,[18] which are source characteristics eminent for obtaining a high degree of coherence at the sample position. At 15 KeV, with the sample 60 m from the source, the coherence length in the vertical direction is typically of the order of ~ 50 μm.[19] The horizontal coherence length, on the other hand, is below the low limit for detecting interference. Accordingly, only sample boundaries with an interface-normal component in the vertical direction should be expected to give rise to a significant phase contrast.

The ID22 undulator emits up to seven harmonics, each having a spectral bandwidth (ΔE) from a few ten to a few hundred of electrovolts for a typical operation in the X-ray regime. Consequently, the unfiltered undulator radiates with a high-power density that can be up to a few W/mm^2 at the sample position. It is, therefore, necessary to attenuate the source by some means in order to reduce the heat load on the sample. For this purpose, there are options available such as high-energy cut-off mirrors or attenuating foils, which can be used in combination. However, if attenuation by the sample is not too strong, monochromatization of the undulator spectrum, yielding a single band (ΔE equal to a few electrovolts), is the best alternative for reducing the heat load without diminishing beam coherence. Monochromatization reduces the heat load to typically a few mW/mm^2, yet a high flux is preserved.

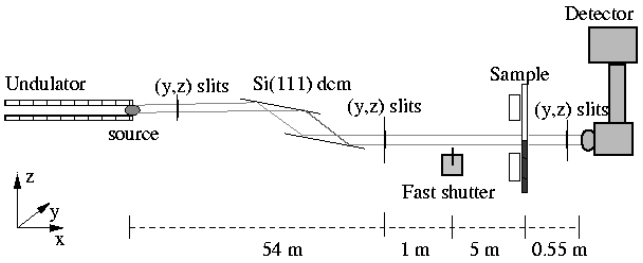

Fig. 1—The equipment setup.

Figure 1 gives a schematic overview of the experimental setup used in the experiments reported here. The beam conditions were defined by a fixed-exit double-flat Si(111)-crystal vertical monochromator and a set of beam-defining slits. The beam path from the source to the sample position is ~ 60 m, of which almost all was pumped to 10^{-6} to 10^{-7} torr, to prevent air scattering/attenuation. In the setup, the sample-to-detector distance was not evacuated and was adjustable from 0.5 to 2.5 m.

2. *The detector system*

The detector system used for the experiments was a Fast Readout Low Noise II (FReLoN 2000) charge-coupled device (CCD)[20] with an area of 2048×2048 pixels, pixel size of ~ 14 μm^2, and a dynamic range of 14 bits. The CCD can be read out in four separate channels at an electronic noise level as low as 1 count/pixel. The images can be stored directly in computer random-access memory, bringing the physical deadtime for a full CCD frame down to ~ 0.35 seconds. It is also possible to read out the array in a 2×2 binning mode, decreasing the deadtime to ≤ 100 ms. The FReLoN 2000 CCD is mounted onto the back focal plane of a visible light-microscope lens system, of which the front focal plane is adjusted to fall into a transparent luminescent screen which converts X-rays to visible light.[21] The screens employed in the experiments were 3.5- and 12.0-μm-thick lutetium aluminum garnet (LAG, $Lu_3Al_5O_{12}$) single-crystal scintillator screens doped with europium and grown on 170-μm-thick yttrium aluminium garnet (YAG) substrates. Selection between different screen thicknesses presents a tradeoff between spatial resolution and detection efficiency; the latter may be decisive for the attainable temporal resolution, and the best alternative will be determined by the sample and the incident photon energy. The LAG:Eu screens are superior to commercially available YAG:Ce screens[21] in work where fast readout is required—after 100 ms, the LAG:Eu afterglow for a 0.1-second exposure is of the order 5×10^{-4}. The LAG quantum efficiency is at its optimum just above the Lu L photoelectric absorption edge at 9.28 KeV, falling off gradually at higher energies.

The lens system is built with an adjustable support which holds 5-, 10-, and 20-times-magnification objectives, mounted so that their focal distances fall approximately in the same plane. A motorized translation of the objective housing serves to optimize the camera focus by adjusting the lens focal distance to fall in the central plane for the X-ray to light events in the luminescent screen. The lens system also consists of a twofold eyepiece and a reflecting

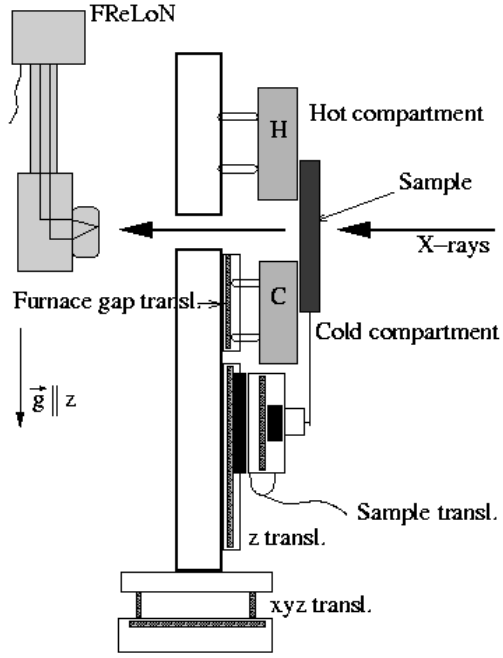

Fig. 2—The furnace rig.

mirror which shifts the visible-light-beam path with respect to that of the X-rays, thus preventing high-energy X-rays, if in use, from reaching the CCD area.

An external fast shutter placed upstream from the sample was connected to the camera triggering, all controlled *via* a dedicated Spec* application. This spec application also offered online image display. In the setup used, the camera spec ran under Solaris on a SUN workstation with 256 MB of extended memory. This limited the maximum number of serial frames acquired to 30 or 120 images in an unbinned or binned readout, respectively. Employing the 3.5-μm-thick luminescent screen, the spatial-resolution limit at 15 KeV was ~0.8 μm. The applicable temporal resolution was somewhat limited by a ~20 Hz periodic transverse displacement of the incident beam due to either monochromator or electron-beam instabilities. In practice, it was, therefore, not beneficial to employ exposure times shorter than 100 to 150 ms. Together with the readout/storage time, the exposure time combined to a minimal time elapse between frames of typically 0.25 or 0.9 seconds for the binned or unbinned mode, respectively.

*Spec is a portable, general-purpose data-acquisition software system provided by Certified Scientific Software at http://www.certif.com.

3. *The furnace system*

The furnace system used in previous studies of solidification processes in the Sn-Pb alloy system[12,13] had to be modified to work satisfactorily at the elevated temperatures required in the work with Al-Cu solidification processes. The furnace system, which is shown in Figure 2, is constructed as a Bridgman apparatus. The hot (H) and cold (C) furnaces are controlled individually, with adjustable internal spacing, and are operated above and below the liquidus and solidus temperatures, respectively, for the sample alloy constitution. Samples are mounted in a sliding holder, which is connected to a motorized translation along *z*, and are constructed so that one side of the sample glass container remains in firm contact with the furnace surfaces during sample translation. The equipment is assembled on a supporting Al rail which is mounted on an *xyz* translation stage, allowing for rapid and accurate alignment of the equipment in the X-ray beam. Both furnaces are made from blocks of aluminium bronze (Cu-10 wt pct Al) and heated with Pt elements, all enclosed in heat-shielding material (not shown in the illustration of Figure 2). The heating-element wires are folded to maximize the contact area and make its contact with the heat blocks uniform. Both furnaces are equipped with internal K thermocouples, which can be logged at 2 Hz through a computer board.

4 *The samples*

Aluminium alloys with 3, 6, 10, 20, and 30 wt pct Cu were prepared from aluminum and copper, both of 99.999 wt pct purity. The metals were melted together in alumina crucibles and cast in an insulating mold chilled at the bottom to promote directional solidification and, thus, to avoid porosity and macrosegregation. Parallel samples from the alloys containing 6 and 10 wt pct Cu were also prepared in a grain-refined state. The grain refinement was accomplished by the addition of an Al-5 wt pct Ti-1 wt pct B rod-type master alloy to the melt in an amount which corresponded to final titanium and boron concentrations of 100 and 20 ppm, respectively. Samples were taken for each alloy from an area 1 cm from the chill and were cut into rectangular 1.5 × 3.0 cm^2 (H × V) slices measuring 180 to 200 μm in thickness after polishing. All samples were preoxidized by heat treatment at 720 K for 2 hours, forming a submicron protective oxide, followed by three different preparation strategies: (1) covering with boron nitride powder followed by a wetting in acetone, (2) coating with boron nitride spray, or (3) oxidation only. Finally, the prepared samples were placed between two 100-μm-thick quartz microscope preparation glasses, which were welded together at their edges to form a sealed sample container. The oxide/BN + oxide scales were necessary to prevent liquid Al from being oxidized in direct contact with the quartz container walls. The motivation for using several alternative sample preparations was that prior to synchrotron X-ray exposure, it was unclear whether any of the BN sample coating techniques would work out, since the coating layers could form structures giving rise to unwanted phase contrast. For all alloy compositions, samples were also prepared with internal 100 μm K thermocouples placed inside the sample containers. The thermoelements were in direct contact with the coated/oxidized sample surface and logged in synchrony with those of the furnace system. Prior to the actual solidification experiments, the samples were placed in the furnace rig and oxidized once more at 720 K for 1 hour, to mend eventual cracks formed in the protective scale during their enclosure in glass.

C. *Experiment Conditions*

Monochromatic photon energies in the range from 12 to 20 KeV were used. Ideally, amplitude contrast would be more pronounced at the CuK photoelectric absorption edge at 8.8980 KeV. However, at this energy, the attenuation length for Al is only 109 μm, which is indeed somewhat short, taking into account a typical sample thickness of 200

μm and also that the beam had to pass through 200 μm of quartz glass (the sample container). Furthermore, even a modest beam path in air would attenuate the beam significantly at such low energies. Accordingly, the incident-beam energy had to be selected as a compromise between an optimized contrast and adequate signal transmission through the sample and air to obtain high spatial and temporal resolutions. Furthermore, energies below the Lu L edge were less suitable, taking the detection efficiency of the scintillator into account. At 15 KeV, the attenuation lengths for Cu, Al, and SiO_2 are 15, 498, and 840 μm, respectively. Numerical evaluation of Eqs. [2] and [3] gives δ_{AL} (15 KeV) = 2.4149×10^{-6}, β_{Al} (15 KeV) = 1.2994×10^{-8}, δ_{Cu} (15 KeV) = 7.6117×10^{-6}, and β_{Cu} (15 KeV) = 4.3778×10^{-7}.

The monochromatic flux at 15 KeV directly after a storage-ring refill was determined to be $\sim 5 \times 10^{12}$ photons/(s·mm^2) at the sample position. Slit systems positioned up- and downstream of the optical elements (Figure 1) were used to define a quadratic beam cross section slitting the beam horizontally to the same size as the full vertical beam, *i.e.*, $\sim 1.35 \times 1.35$ mm^2 at the sample.

During the experiment, the sample-to-detector distance was fixed at 55 cm. The camera was read out in the four-channel mode, varying between the unbinned and 2×2 binned modes. Alternation between the binned and unbinned readout, combined with the 10- and 20-times-magnification objectives, was used to produce different experimental conditions with respect to spatial and temporal resolutions. A 10-times-magnification objective and a binned readout gave time costs for readout/storage of $t_{rs} = 100$ ms, which, at minimal exposure times, t_{exp}, resulted in a temporal resolution of 0.25 seconds, with a spatial resolution of ~ 2.5 μm and a memory capacity for collecting 120 serial frames. A spatial resolution of ~ 1.0 μm could be achieved using the 20-times-magnification objective/unbinned readout, but, as the unbinned readout requires $t_{rs} \simeq 0.4$ s and also generally longer exposure times, the applicable temporal resolution in this camera configuration was limited to ~ 0.9 seconds, with a memory capacity for 30 serial frames. Using the 10-times-magnification objective, the camera field of view was approximately identical to the full vertical beam size, 1.4×1.4 mm^2.

The furnace temperatures were varied in ranges of T_H = 850 to 990 K and T_C = 700 to 840 K for the H and the C compartments, respectively, while their internal spacing, Δz, was varied in the range from 2 to 9 mm. This resulted in mean temperature gradients over the sample of $\langle G \rangle = ((T_H - T_C)/\Delta z) \in (15.0, 135.0)$ K/mm. Tests of furnace-temperature stability were conducted using a sample with an internal thermocouple. The couple was positioned well inside the H compartment and moved with a constant speed to a final position well inside the C compartment, logging the temperature of the sample couple and both furnaces twice per second. This test confirmed that the thermal contact between the furnaces and the sample was stable and uniform, and that the thermal gradient in the gap between the furnaces was constant within measurement accuracy. Accordingly, the mean temperature gradient within the field of view, G, could be estimated by its overall mean, $\langle G \rangle$.

Acquisition of a solidification series was initiated from a sample positioned in the upper hot furnace, placed sufficiently in contact to melt the whole sample. Then, it was moved in the $-z$ direction toward the cold compartment at a constant velocity in the range from 3.2 to 80 μm/s. Nucleation, followed by the evolution of a growth front propagating along the thermal gradient, took place as soon as a firm thermal contact between the glass container and the cold compartment was established. With the spec online image display continuously updating itself, the acquisition of images in the computer memory could be started as soon as the solidification front appeared in the field of view. Experimental parameters were fine-tuned during subsequent collections of solidification series, but only in a few cases was it possible to obtain parameters and reproduce the solidification process accurately enough to collect a full 120-image series over a front while maintaining a stationary field of view. The sample preparation techniques employed gave quite different results with respect to sample lifetimes and unwanted structures/image contrasts. Both types of BN-coated samples sustained at least 5 to 10 times as many melting/solidifying cycles compared to samples that had been oxidized alone, the former being more inert toward reactions between the melt and the glass container. Furthermore, the BN spray coating turned out to be the best preparation alternative, even though the coating layer appeared thicker compared to those obtained with the BN/acetone coating. The latter preparation alternative was rather unsuccessful, leaving coating-layer structures in the images. In total, 137 image series of solidification processes were collected, adding to a total of $\sim$40 GB of raw data.

III. RESULTS

It became obvious at an early stage of the imaging experiments that the contrast from the samples with 3 and 6 wt pct Cu was marginally low. When more contrast was obtained for samples with higher Cu contents, it was due to the formation of a quasi–two-dimensional (2D) segregated solidified structure confined between the container walls giving rise to amplitude contrast. Likewise, a 2D contrast appeared at the solidifying front, due to amplitude contrast arising from the constitutional difference between the liquid and the growing dendrites combined with phase contrast due to the discontinuity in density and composition at the liquid-solid boundary. In samples with 30 wt pct Cu, pure phase contrast was also observed as a visible isothermal eutectic front. In the low-Cu-content alloys, the amount of interdendritic structure was too small to fill in volumes between the container walls as continuous zones; accordingly, less amplitude and phase contrast resulted, since a beam-path integration along x would tend toward an average over the separate constitutional domains and, therefore, would not give rise to any strong contrast in $A(y, z)$ and $\phi(y, z)$ (Eqs. [5] and [6]). Attempts to enhance the contrast of these frames by image processing also enhanced artifacts, mainly from oxide irregularities, present in the images and did not improve the information content significantly. Therefore, only results from the alloys with 10, 20, and 30 wt pct Cu are presented here.*

*The solidification images presented will also be made available in animated GIF sequences downloadable from http://www.phys.ntnu.no/~ragmat/index.html.

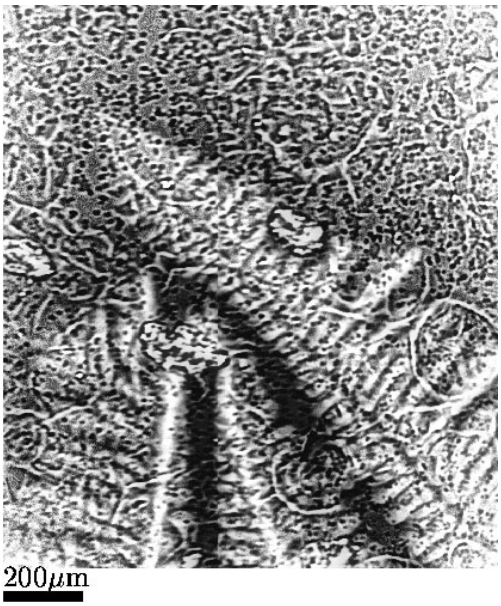

(*a*)

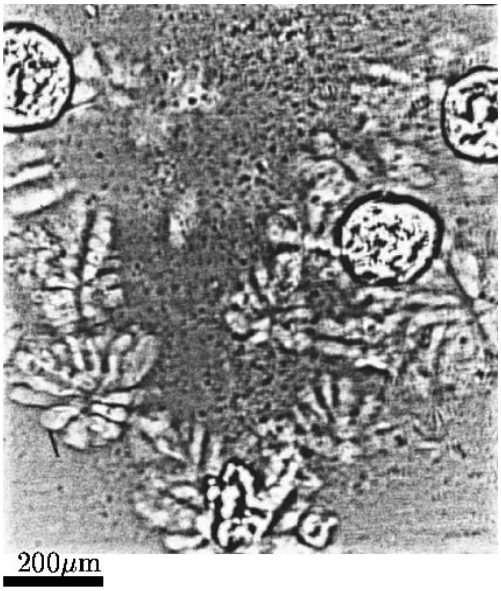

(*b*)

Fig. 3—Crystal growth in Al-10 pct Cu. (*a*) Columnar dendritic growth in the nongrain-refined state. Binned readout, cropped image field of view, $CIFV = 1.11 \times 1.26$ mm^2 (H × V), $G \sim 105$ K/mm, $t_{exp} = 0.35$ s/frame, and $v_s = 32$ μm/s. (*b*) Equiaxed cellular-dendritic growth in the grain-refined state. Circular features are traces in the oxide from gas bubbles formed under earlier solidification experiments with the sample. Unbinned readout, $CIFV = 0.95 \times 1.05$ mm^2, $G \sim 55$ K/mm, $t_{exp} = 0.2$ s/frame and $v_s = 16$ μm/s.

A. *Dendritic Solidification*

Figure 3 shows images from the Al-10 pct wt Cu alloy in the nongrain-refined and grain-refined state. Even though the images still contain artifacts, it can be seen that the resolution is high enough to observe details of the growing-crystal morphologies, like dendrite-arm spacing, dendrite-tip size, *etc.* It can also be seen from Figure 3(b) that the grain refinement has been very efficient; the number of grains is, in fact, so large that individual crystals overlap, which makes measurements of front propagation difficult. It can, nevertheless, be seen in the grain-refined sample that well-developed grains with orthogonal arms do not form; the grains can, rather, be characterized as equiaxed cellular crystals. The growth of such crystals is not well known[22] and will be subject to further investigations.

Figure 4 shows a sequence from an imaging experiment with the Al-20 wt pct Cu alloy. It can be seen that the alloy grows in a columnar way, but that dendrite fragments, primarily ternary arms, melt off the dendrite and form new crystals. Grain formation by dendrite fragmentation is a known phenomenon, and several mechanisms have been proposed. Figure 4 shows, on the lower-right-hand side, how dendrite arms detach by remelting at the root. The figure also shows that the newly formed crystals have a lower density than the copper-rich melt and, therefore, float upward until they grow to a size where they are too large to move freely between the glass walls of the sample container. Grain multiplication induced by dendrite fragmentation, like that illustrated in Figure 4, was observed in several solidification experiments with the 10, 20, and 30 wt pct Cu samples.

Figure 5 shows a sequence from equiaxed growth in Al-30 wt pct Cu. In this sample, the constitutional undercooling due to the high alloying concentration has been large enough for impurity particles in the melt to nucleate new dendrites. It can be seen that these dendrites are well developed and form orthogonal arms quite early during growth. The images also show eutectic growth. The composition of the sample (30 wt pct Cu) is quite close to the Al-Cu eutectic composition at 33 wt pct Cu. With $G = 30$ K/mm, one would expect primary aluminum growth and eutectic growth to be observed in the same field of view, since the equilibrium liquidus temperature of the alloy is only 15 K above the eutectic temperature. It can be seen that the position of the eutectic in the sequence is changing; the eutectic is, in fact, growing upward in the image, showing isotherms that are moving with respect to the imaging system. The eutectic shows quite heavily segregated dark columnar regions, which must relate to an uneven distribution of Cu. From the animation of the series, it can be observed from their dynamics that these Cu columns do not solidify with the eutectic. The location and density of such columns is not arbitrary; based on this and a similar series with equiaxed growth, their appearance is found to relate to the presence and amount of dendrites. At present, the true nature of this phenomenon is not clear. However, one may speculate that thin Cu films may form between growing equiaxed dendrites and the glass container due to chemical diffusion directed predominantly parallel or antiparallel to the X-ray beam, and that these films are entrapped between the solidified eutectic and the glass. This particular sample was not treated with BN, and could not, therefore, sustain the number of melting/solidifying cycles required to stabilize the isotherm. With BN-spray-coated samples, a quite stable temperature field could be achieved, as shown in Figure 6, which presents columnar solidification of Al-30 wt pct Cu.

B. *Eutectic Growth*

Figure 7(a) shows eutectic growth in Al-30 wt pct Cu. The images of this experiment did not show any primary aluminum dendrites. One explanation for this absence of dendrites is macrosegregation, which may have occurred

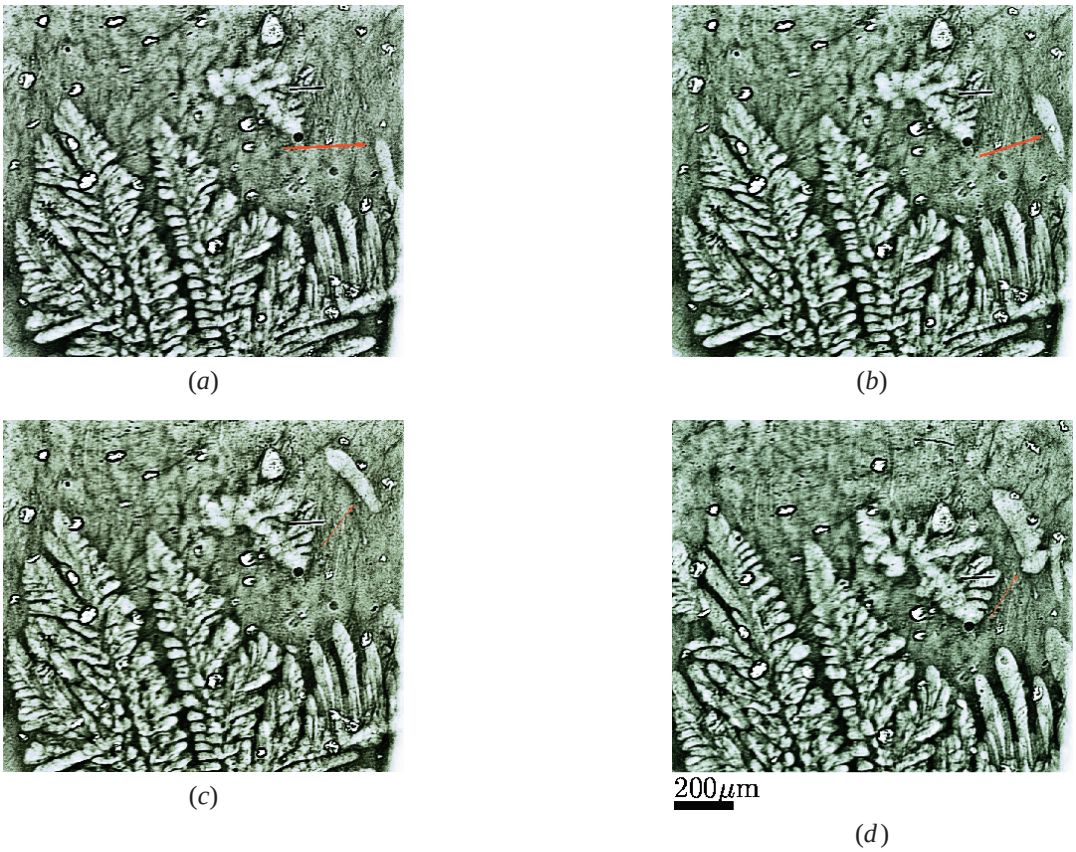

Fig. 4—Dendritic growth and grain multiplication in Al-20 wt pct Cu. The upper central part of the images show a grain that originated from a ternary arm detaching from the columnar front at the beginning of the image series acquisition. At this stage, several new branches have developed. To the right, the image series captures the formation of a new grain (red arrows). (*a*) Just after a ternary arm detachment, t_0. (*b*) The upward floating of the detached grain four images later at $t_0 + 2.0$ s. (*c*) The grain has grown to a size that confines it between the sample container glass walls at $t_0 + 10$ s. (*d*) At $t_0 + 34$ s, the grain has grown further in size, and another ternary arm has loosened and floated up at its right. For all images: binned readout, $CIFV = 1.29 \times 1.13$ mm^2, $G \sim 37$ K/mm, $t_{exp} = 0.3$ s/frame, and $v_s = 6.4$ μm/s.

due to the buoyancy of the aluminum crystals resulting in positive copper segregation at the bottom of the sample. Another reason may be that the gradient and low growth rate in the experiment stabilized the growth of a planar eutectic growth front at the near-eutectic concentration. The limiting growth rate for a planar front (no constitutional undercooling) of a eutectic growth front is[23]

$$V \leq \frac{GD}{m(C_0 - C_e)}, \qquad [7]$$

where V is the growth velocity, m is the liquidus slope, C_0 is the alloy concentration, and C_e is the eutectic concentration. In the present case, $G = 4.5 \times 10^4$ K/m, $D = 3.5 \times 10^{-9}$ m^2/s,[12] $m = -4.9$ K/wt pct,[21] $C_0 = 30$ wt pct, and $C_e = 33.1$ wt pct,[21] which gives a limiting growth rate of about 10 μm/s. The actual growth rate in the experiment was 7 μm/s, so a planar eutectic growth front, as seen in Figure 7(a), is to be expected. If the growth rate is increased and/or the temperature gradient decreased, the planar eutectic front would be destabilized. This is shown in Figure 7(b), where the growth rate has been increased to 32 μm/s, the temperature gradient being fairly the same. The growth front is no longer planar, but has formed eutectic cells.

In samples without the BN barrier, reactions between the aluminum melt and quartz glass resulted in significant silicon concentrations in the melt. Figure 8 shows solidification in a sample where the silicon concentration has exceeded about 9 wt pct, where, according to the ternary Al-Cu-Si phase diagram, primary silicon is solidified from an aluminum melt with 10 wt pct Cu.[24] Primary silicon crystals can be seen in addition to growth of an Al-Si eutectic which is highly branched, and a facetted silicon phase leads the growth of the eutectic.

C. *Porosity*

Porosity was observed in many samples during solidification. The pores had a round shape and were presumably due to segregated hydrogen bubbles formed during solidification.[25]

Normally, these bubbles formed relatively early during solidification and could escape, either through flotation or by diffusion out at the side of the thin sample. An example of pore formation in an Al-30 wt pct Cu alloy is shown in Figure 9, where solidification is taking place downward and the solidification front prevents flotation of the bubbles. It can be seen that, in this case, the pores form during the eutectic reaction and, therefore, get an elongated shape. This is to be expected, since a simple calculation from the Scheil equation shows that the dendrites in this alloy only make up 10 pct of the volume, and the melt becomes supersaturated with hydrogen only later during the eutectic solidification.

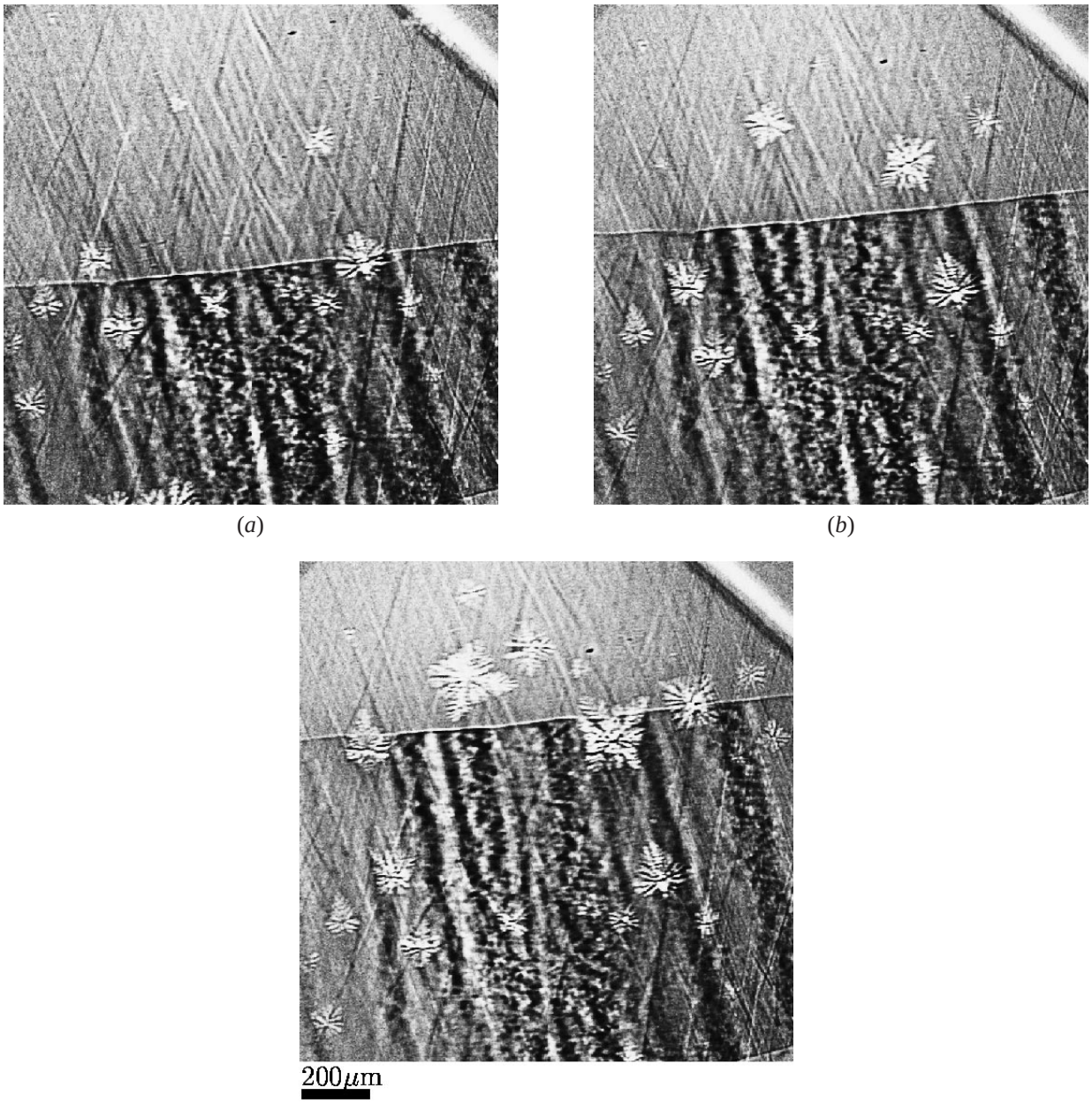

(*a*) (*b*) (*c*)

Fig. 5—Equiaxed dendritic and planar eutectic growth in Al-30 wt pct Cu. The images show formation and growth of equiaxed dendrites preceding the planar eutectic front. The black and white diagonal stripes in the upper right corner are artifacts left after image processing and due to a temporary misalignment of the furnace rig and camera with respect to the fast shutter placed upstream (Fig. 1). (*a*) t_0, (*b*) four frames later, at $t_0 + 1.4$ s, and (*c*) six frames later, at $t_0 + 2.1$ s. Parameters: binned readout, $CIVF = 1.4 \times 1.4$ mm^2, $G = 30$ K/mm, $t_{exp} = 0.15$ s/frame, and $v_s = 50$ μm/s.

The solidification images presented here have been processed with various filters. Several routines have been specially designed to carry out image processing directly on the 16-bit gray-level format of the raw data, such as flat-field corrections, noise filtering, and adaptive contrast enhancement, before conversion to a standard 8-bit format. Further processing and coloring have been carried out using the Gnu Image-Manipulation Programs.[26]

IV. DISCUSSION

As illustrated by the figures, the image series collected were phenomenologically rich. In addition to the results presented, the effects on grain formation, growth, transport, and annihilation and those due to gravity and convective currents were observed and could be interesting topics for more systematic studies.

In contrast to the earlier solidification studies in the Sn-Pb alloying system,[12] the Al-Cu system was suited to take full advantage of the attainable temporal and spatial resolutions. In the latter studies, the limits in performance were set by the detector system and the X-ray source characteristics rather than by the sample material. The simultaneous high resolutions obtained in this experiment exceed those obtained with other X-ray transmission electron microscopy techniques[6–9] by more than one magnitude, both spatially

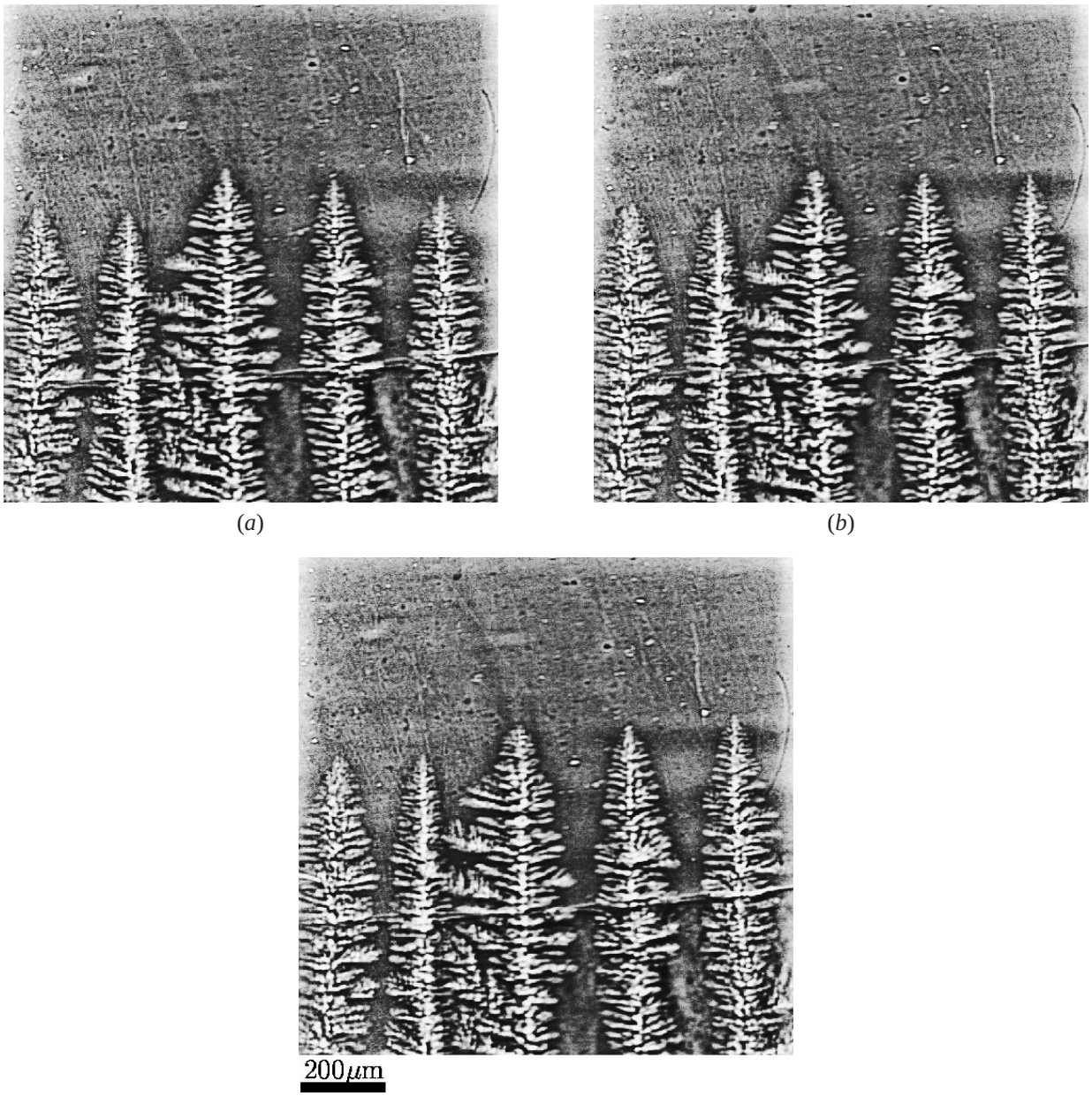

(*a*) (*b*) (*c*)

Fig. 6—Columnar dendritic and planar eutectic growth in Al-30 wt pct Cu. Columnar dendrites proceeded by a planar eutectic front visible as a nearly horizontal line located roughly in the middle between the dendritic front and the bottom of the images. (*a*) t_0, (*b*) three frames later at $t_0 + 1.5$ s; and (*c*) six frames later at $t_0 + 3.0$ s. Parameters: binned readout, $CIFV = 1.13 \times 1.13$ mm^2, $G = 27$ K/mm, $t_{exp} = 0.3$ s/frame, and $v_s = 22.4$ μm/s.

and temporally. The ability to exploit the local variations in refraction by the sample as another source of contrast in addition to attenuation is unique in work with solidification-process monitoring.

The primary focus for this work has been to develop an experimental technique for *in-situ* studies of dendritic growth in metallic alloys. The results obtained with solidifying alloys from the Al-Cu system come close to what is achievable at present. Algorithms to extract physicochemical parameters decisive to the solidification processes from experiments such as this are, however, not established yet. Currently, efforts are made in developing suitable edge-detection modules to extract co-ordinates and propagation-velocity fields for a 2D projection of the dendritic solid-liquid interface. This should be followed with filters to analyze the relative X-ray transmission, in order to extract and interpolate contours for a local liquid constitution ahead of the interface. A modeling algorithm for dendritic growth utilizing data extracted from the experiment is also required. Experimental mapping of the interface morphology and propagation, together with measurements of concentration gradients in constitutionally undercooled quasi-2D systems, opens the door, in principle, to estimation of 2D diffusion locally, thus providing a means to study the onset and effect of interactions among adjacent interfacial features. When the required image-processing and modeling tools have been established, there are several critical aspects concerning the experimental design and limit in performance which need to be addressed. The limits in spatial and, especially, temporal resolutions may be too coarse in comparison to those applied

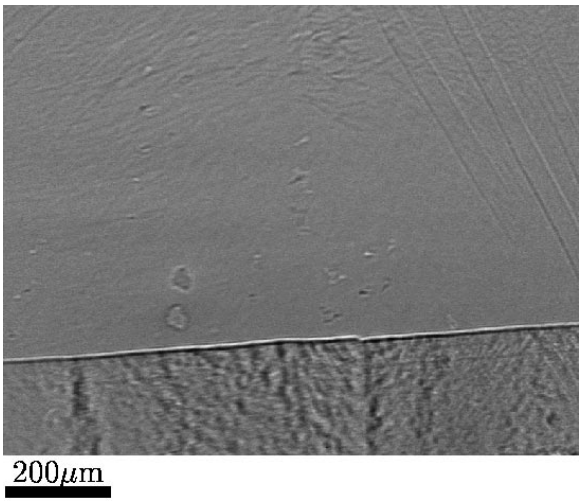

(*a*)

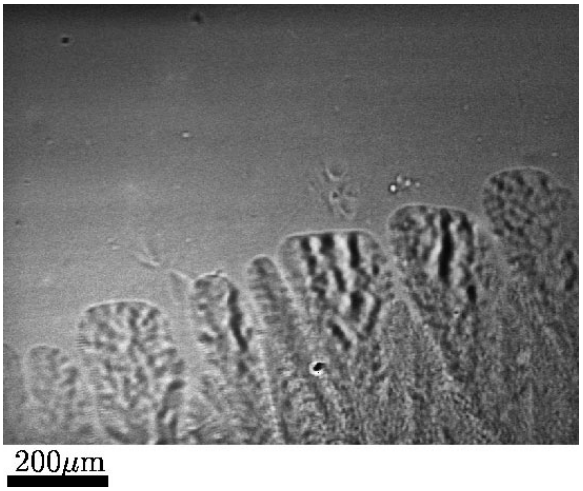

(*b*)

Fig. 7—Planar and cellular eutectic growth in Al-30 wt pct Cu. The eutectic fronts appear almost entirely as phase contrast objects. (*a*) Planar eutectic front at a growth rate below the limit of morphological stability. Binned readout, $CIFV = 1.06 \times 0.82$ mm^2, $G = 46$ K/mm, $t_{exp} = 0.3$ s/frame, and $v_s = 6.4$ μm/s. (*b*) Cellular eutectic front growing at a rate above stability limit. Binned readout, $CIFV = 1.1 \times 0.83$ mm^2, $G = 37.5$ K/mm. $t_{exp} = 0.3$ s/frame, and $v_s = 32$ μm/s.

in *ab initio* numerical modeling of dendritic growth (References 4 and 5 in Reference 12), and whether they are adequate to support any modeling at all remains an open question.

Apparently, a critical factor regarding the general validity of the experimental method for describing solidification fundamentals is due to the effects caused by the confinement of the solidifying system between the glass walls of the sample container. This confinement clearly affects the growth itself, as demonstrated by the entrapment of detached grains in Figure 4, but is also likely to affect liquid convection and solute transport and will, in some cases, influence nucleation rates.[12] However, for the enhancement of image contrast, a quasi-2D character of the sample is advantageous. As long as image analysis is carried out taking the experimental restrictions into account, it is clear that observations made in two dimensions of a specific quasi-2D system can be of value outside the system itself. Similar restrictions

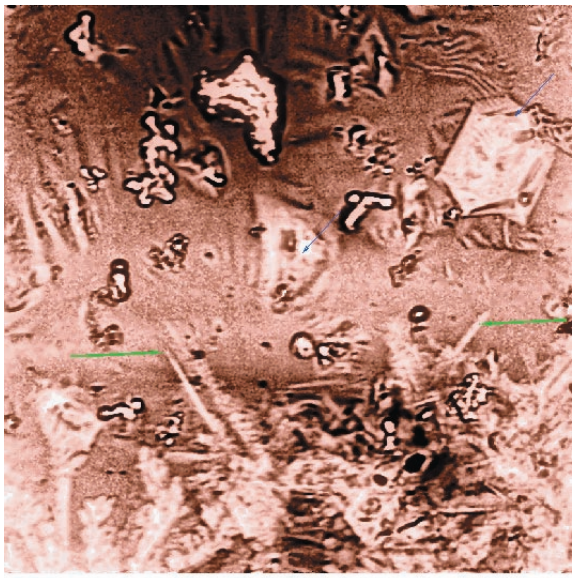

Fig. 8—Solidification processes in the ternary Al-Cu-Si system. The image shows the growth of a branched Al-Si eutectic (lower region), primary silicon crystals (blue arrows), and a facetted silicon face preceding the eutectic front (green arrows). Binned readout, $CIFV = 1.13 \times 1.13$ mm^2, $G = 103$ K/mm, $t_{exp} = 0.3$ s/frame, and $v_s = 16$ μm/s.

apply in work with transparent analogs,[27] from which valuable information on dendritic growth has been extracted frequently for over three decades. Restrained dendritic growth also occurs in many real castings. Furthermore, numerical modeling in two dimensions has been carried out repeatedly and demonstrated to be of general applicability (Reference 4 in Reference 12).

In principle, the method given here can be applied to study solidification processes in other alloying systems. The method will be suited primarily for binary systems, for which an X-ray photon energy can be chosen to produce a short attenuation length for the alloying element with respect to that of the base metal. Essential problems which have to be solved separately for each system are the preparation of the sample itself and the use of a fairly X-ray-transparent, inert, and phase-contrast-free sample container.

V. CONCLUSIONS

The application of third-generation intense and coherent synchrotron X-rays and high-performance detector systems for time-resolved *in-situ* X-ray imaging studies of metal solidification processes has promising potential. Further developments in postexperimental analysis and modeling are required to extract quantitative results. Future experimental studies should be dedicated toward a more systematic mapping of solidification under various conditions. In order to improve further on the spatial and temporal resolutions, new and improved detector systems are required. At present, the flux of the incident X-ray beam can be increased by a few orders of magnitude, going from a monochromatized to an attenuated undulator beam; hence, experiments with less-X-ray-transparent alloys are feasible. However, shorter exposure times cannot be applied with a higher flux, due to spatial instabilities of the X-ray source. A solution to this

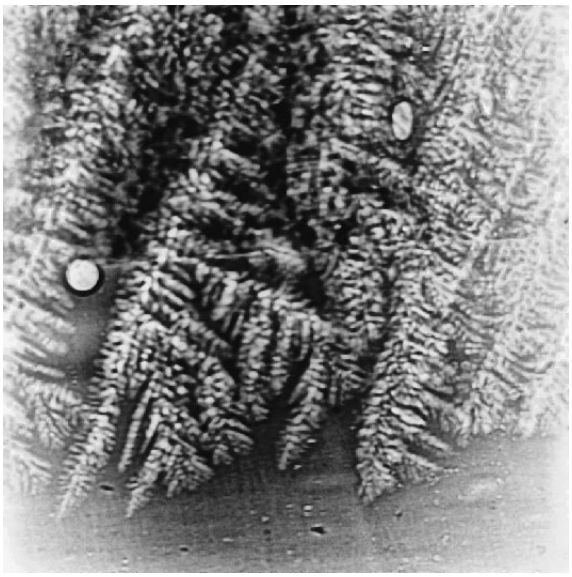

(*a*)

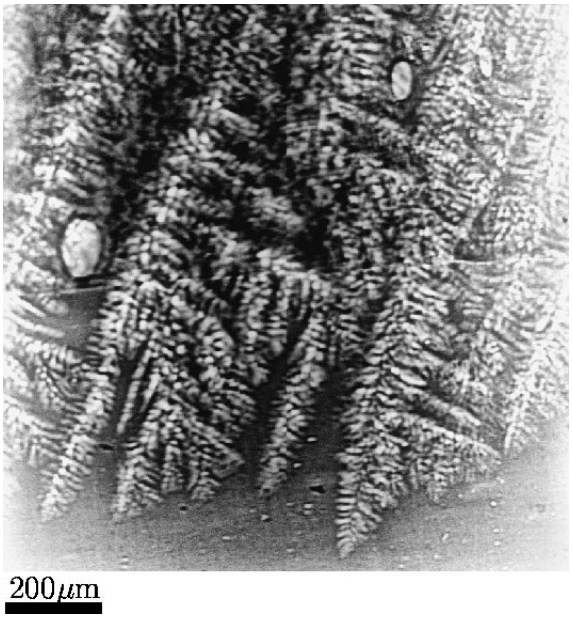

(*b*)

Fig. 9—Formation of pores in Al-30wt pct Cu. Three pores are visible, one gas bubble in the left middle as it gets captured and shaped into an elongated pore in the eutectic solid and two pores resident in the solid in the upper right corner. (*a*) Spherical gas bubble just ahead of the eutectic front and (*b*) an elliptically shaped pore has formed in the solid seven frames or 3.5 s later. Binned readout, $CIFV = 1.13 \times 1.13$ mm^2, $G = -26.8$ K/mm, $t_{exp} = 0.3$ s/frame, and $v_s = 22.4$ μm/s.

problem would require improvements in the performance of the magnetic lattice controlling the synchrotron electron beam.

ACKNOWLEDGMENTS

This work has been supported by the Norwegian Academy of Sciences 85/2000 and by Halvor B. Holtas legacy 338/2000. We express our gratitude to David Fernandez, ESRF, for his assistance in customizing Spec software applications for the image acquisition.

REFERENCES

1. Ø. Nielsen, L. Arnberg, A. Mo, and H. Thevik: *Metall. Mater. Trans. A*, 1999, vol. A30, pp. 2455-462.
2. Ø. Nielsen, B. Appolaire, H. Combeau, and A. Mo: *Metall. Mater. Trans. A*, 2001, vol. A32, pp. 2049-60.
3. S.W. Chen and C.C. Huang: *Acta Mater.*, 1996, vol. 44, pp. 1955-65.
4. M.E. Glicksman, R.J. Schaefer, and A.J. Ayers: *Metall. Trans. A*, 1976, vol. A7, pp. 1747-59.
5. W. Losert, B.Q. Shi, and H.Z. Cummins: *Proc. Nat. Acad. Sci. USA*, 1998, vol. 95, pp. 431-38.
6. M.R. Bridge, M.P. Stephenson, and J. Beech: *Met. Technol.*, 1982, vol. 9, pp. 429-33.
7. W.F. Kaukler, F. Rosenberger, and P.A. Curreri: *Metall. Mater. Trans. A*, 1997, vol. A28, pp. 1705-10.
8. P.A. Curreri and W.F. Kaukler: *Metall. Mater. Trans. A*, 1996, vol. 27A, pp. 801-08.
9. W.F. Kaukler and F. Rosenberger: *Metall. Mater. Trans. A*, 1994, vol. 25A, pp. 1775-77.
10. T. Matsumiya, W. Yamada, T. Ohashi, and O. Nittondo: *Metall. Trans. A*, 1987, vol. A18, pp. 723-27.
11. G. Grange, J. Gastaldi, C. Jourdon, and B. Billia: *J. Cryst. Growth*, 1995, vol. 151, pp. 192-99.
12. R.H. Matheisen, L. Arnberg, F. Mo, T. Weitkamp, and A. Snigirev: *Phys. Rev. Lett.*, 1999, vol. 83, pp. 5062-65.
13. L. Arnberg, R.H. Mathiesen and F. Mo: *Proc. M.C. Flemings Symp. on Solidification and Materials Processing*, R. Abbaschian, H. Brody, and A. Mortenson, eds., TMS, Warrendale, PA, 2001, pp. 385-89.
14. D.R. Poirier and S. Ganesan: *Mater. Sci. Eng. A*, 1992, vol. A157, pp. 113-23.
15. R.W. James: in *The Optical Principles of the Diffraction of X-Rays*, L. Gilmore, ed., G. Bell and Sons, London, 1948, pp. 137-38.
16. P. Cloetens, R. Barrett, J. Baruchel, J.-P. Guigay, and M. Schlenker: *J. Phys. D. Appl. Phys.*, 1996, vol. 29, pp. 133-46.
17. A. Snigirev, I. Snigireva, V. Kohn, S. Kuznetsov, and T. I. Schelokov: *Rev. Sci. Instrum.*, 1995, vol. 66, pp. 1-7.
18. *ESRF Beamline Handbook*, USRF User Office, Grenoble, France, 2001, www.esrf.fr/exp facilities/ID22/handbook.html
19. V. Kohn, I. Snigireva, and A. Snigirev: *Phys. Rev. Lett.*, 2000, vol. 85, pp. 2745-48.
20. J.-C. Labiche, J. Segura-Puchades, D. van Brusel, and J.P. Moy: *ESRF Newslett.*, 1996, vol. 25, p. 41.
21. A. Koch, C. Raven, P. Spanne, and A. Snigirev: *J. Opt. Soc. Am. A*, 1998, vol. A15, pp. 1940-51.
22. L. Bäckerud and M. Jansson: in *Light Metals*. W. Hale, ed., TMS, Warrendale, PA, 1996, pp. 679-85.
23. W. Kurz and D.J. Fisher: *Fundamentals of Solidification*, 3rd ed., Trans Tech Publication, Aedermannsdorf, Switzerland, 1989, pp. 101 and 294.
24. H.W.L. Phillips: *Annotated Equilibrium Diagrams of Some Aluminium Alloy Systems*, The Institute of Metals, London, 1951, p. 41.
25. T.A. Engh: *Principles of Metal Refining*, Oxford University Press, Oxford, United Kingdom, 1992, pp. 197-207.
26. O. Kylander and K. Kylander: *GIMP: The Official Handbook*, T. Zuccarini, ed., The Coriolis Group, Scottsdale, AZ, 1999.
27. J.C. LaCombe, M.B. Koss, and M.E. Glicksman: *Phys. Rev. Lett.*, 1999, vol. 83, pp. 2997-3000.